Supplementary Information for "Redox processes at a nanostructured interface under strong electric fields"

Wolfram Steurer, Svetlozar Surnev, Falko P. Netzer

Surface and Interface Physics, Institute of Physics, Karl-Franzens University Graz, A-8010 Graz, Austria

Luca Sementa, Fabio R. Negreiros, Giovanni Barcaro, Nicola Durante, Alessandro Fortunelli

CNR, Consiglio Nazionale delle Ricerche, I-56124 Pisa, Italy

1. Details of theoretical modeling

Density-functional theory (DFT) calculations were performed technically analogous to those reported in Ref.[1] with the addition of an external electric field. They used the QUANTUM ESPRESSO package,[2] employing a basis set of plane waves, ultrasoft pseudopotentials,[3] and the Perdew-Burke-Ernzerhof (PBE) exchange-correlation (xc-) functional.[4] All the calculations were performed spin polarized by applying a pure DFT approach or a DFT + *U* approach;[5] in the latter case the value of *U* on the Ni atoms was chosen between 4.0 and 5.3 eV .[6] The first-neighbor distance in the metal support was set to 2.94 Å, corresponding to the equilibrium lattice parameter of bulk Ag according to our DFT approach, to be compared with an experimental value of 2.89 Å. The metal support was modeled by four Ag slabs in (100) stacking kept frozen in their bulk lattice positions, whereas the oxide monolayer was relaxed until the forces on the oxide atoms resulted in smaller than 0.01 eV/Å. Along the *z* axis, a minimum empty space of 15 Å was chosen to avoid interactions between replicated cells. A dipole correction[7] was applied to cancel spurious Coulombic interactions among replicated images. Values of 40 and 240 Ry were chosen as the energy cutoff for the selection of the plane waves for the description of the wave function and the electronic density, respectively. In the case of small unit cell (containing only four Ni and four O atoms) the first Brillouin zone was *k* sampled by employing a (4,4,1) grid, and the electronic levels were broadened with a Gaussian smearing of about 0.03 eV.

In a first attempt, we performed extensive static DFT simulations, i.e., we solved the electronic structure problem and allowed for structural local optimizations of the NiO/Ag(100)-(2x1) ultrathin film in the presence of an electric field with variable strength. These were performed both for the ground state configuration and in reaction path simulations in which the lowest-energy mechanisms for detachment of an oxygen atom or an oxygen molecule were searched for. In the former case, geometry optimization was unconstrained, i.e., fully relaxed. In the latter, geometry optimization was partially constrained, in the sense that the positions of the outgoing O atom or O_2 molecule were fixed and the other degrees of freedom optimized. In these simulations, the unit cell in the x,y directions was enlarged up to 8 times (i.e., 2x4 times in the two orthogonal directions) to minimize the interaction between "defects" in replicated images. As a result of these simulations we found a reduction in the reaction energy barrier due to the presence of the external electric field (consistent with previous work, see e.g. Ref. 37 in the main text), but to an extent insufficient to rationalize the experimental observation of the reduction of the NiO phase at temperatures lower than 400 K: the oxygen detachment barrier never dropped below 2.5 eV. This proved the limitation of a static modelling, and the need of an out-of-equilibrium transport approach. The predictive accuracy of DFT energetics was however used in a second effort to extract the parameters needed in effective Hamiltonians as those used in DEA.

To match these calculations with the theory of electron/diatomic-molecule DEA, both an electronic and a nuclear Hamiltonian need to be defined.

Let's start with the electronic Hamiltonian first. In the delta-function potential model of a biatomic molecule[8] one assumes for the electron/nucleus interaction potential the following form: $[V(x) = -V_A\,\delta(x - X_A) - V_B\,\delta(x - X_B)]$ where $\delta(x)$ is a delta-function, and appropriate values are selected for V_A and V_B (0.75 and 1 a.u., respectively), so that an analysis of the charge on the two atoms gives ±0.8 units of electron charge – i.e. the same values obtained from a Lowdin charge analysis of DFT calculations on the real NiO/Ag(100)-(2x1) phase. The delta-potential molecule predicts as the ground state of a single electron a bonding orbital of energy $\varepsilon_b(R)$ which is a simple linear combination of two Slater basis functions: [8]

$$\phi_b(x) = c_A(R)\exp(-\gamma(R)\,|x - X_A|) + c_B(R)\exp(-\gamma(R)\,|x - X_B|) \qquad \text{(S1)}$$

where $\gamma(R)$ is the exponent of the bonding orbital and depends smoothly on the inter-nuclear distance R, and $c_A(R)$, $c_B(R)$ are appropriate coefficients also depending on R. The Slater form of the basis functions for $\phi_b(x)$ resembles the solution of the Coulombic hydrogenoid problem and – together with a roughly correct energetics – justifies the use of a delta-potential model. This system also possesses an anti-bonding orbital, which however disappears at finite values of R and whose interpretation and link to real molecules is debatable.[8] A better description of the resonance responsible for electronic capture[9] is obtained by constructing an anti-bonding localized orbital with energy $\varepsilon_a(R)$ as:

$$\phi_a(x) = d_A(R) \exp(-\gamma(R)\,|x - X_A|) - d_B(R) \exp(-\gamma(R)\,|x - X_B|) \qquad \text{(S2)}$$

where $d_A(R)$, $d_B(R)$ are chosen so that $\phi_a(x)$ is normalized and orthogonal to $\phi_b(x)$. Note that we neglect electron-electron interactions and focus on the process in which the incoming electron is captured by the anti-bonding orbital of the delta-potential molecule.

We now need to single out in the real system – i.e. the full NiO/Ag(100)-(2x1) phase – the $\phi_a(x)$ and $\phi_b(x)$ orbitals and their respective energies. An analysis of the system band structure at the Gamma point gives us an orbital which is localized on NiO and has antibonding character lying at 1.85 eV above the Fermi level, see Fig. S1(a), and another orbital which is also mostly localized on NiO and has bonding character lying at 1.86 eV below the Fermi level, see Fig. S1(b).

Once the electronic problem is solved, its output can be used to construct the PES on which the nuclear motion occurs in the Born-Oppenheimer approximation. For example, the total energy of the system in the initial configuration (an incoming electron with momentum k and the AB molecule in its electronic and vibrational ground state) is: $E_i = 2\,\varepsilon_b(R_0) + \mathrm{Rep}(R_0) + k^2/2 + E_{ZP}$, where R_0 is the AB equilibrium distance (around 2 a.u. as projected from the NiO height difference), $\mathrm{Rep}(R)$ is the nuclear repulsion, chosen as to give a Morse profile for the binding $\mathrm{PES_i}(R)$ of the neutral AB molecule similar to the binding energy curve of the NiO outermost pair in the full NiO/Ag(100)-(2x1) phase, and E_{ZP} is the zero-point vibrational energy. In the final configuration of the AB^- system the nuclei move on a PES given by: $\mathrm{PES_f}(R) = 2\,\varepsilon_b(R) + \mathrm{Rep}(R) + \varepsilon_a(R)$. To construct this $\mathrm{PES_f}(R)$ we take $\varepsilon_a(R)$ from the previous analysis of the system band structure, we include the effect of the external electric

field on charge-separated species (only around the equilibrium geometry R_0 without considering asymptotic behaviour, as the cross-section matrix element is concentrated here) and finally estimate an image-charge contribution stabilization of 2.1 eV around R_0.

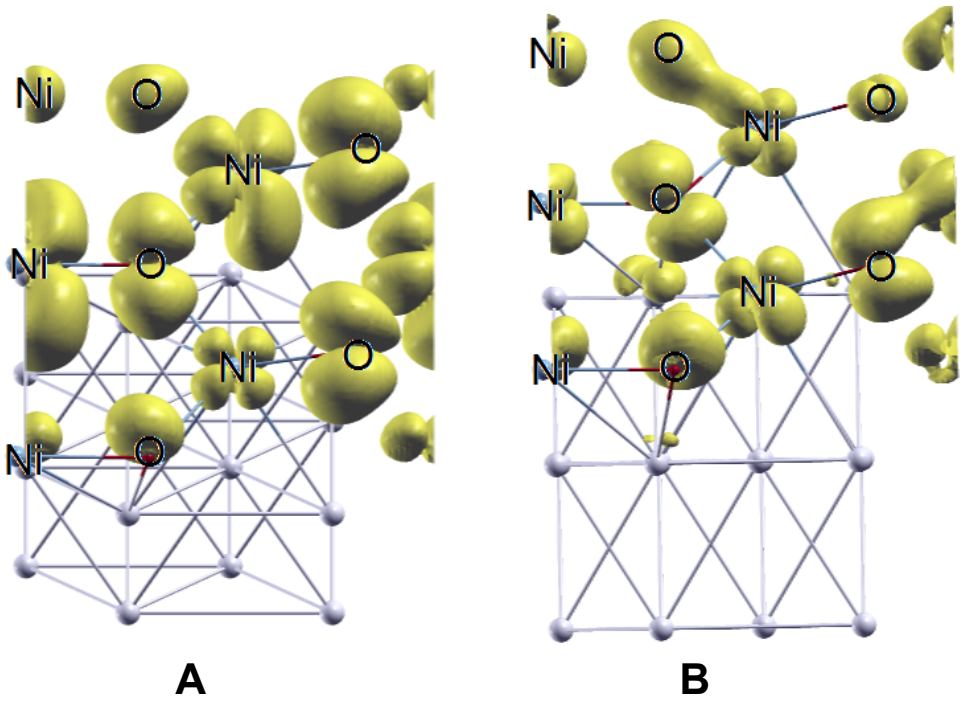

Fig. S1 Density plots of orbitals in the NiO/Ag(100)-(2x1) phase as derived from an analysis of the band structure at the Gamma point corresponding to (**A**) the antibonding ϕ_a and (**B**) the bonding ϕ_b orbitals of the model electronic Hamiltonian.

2. Estimate of the experimental reduction efficiency

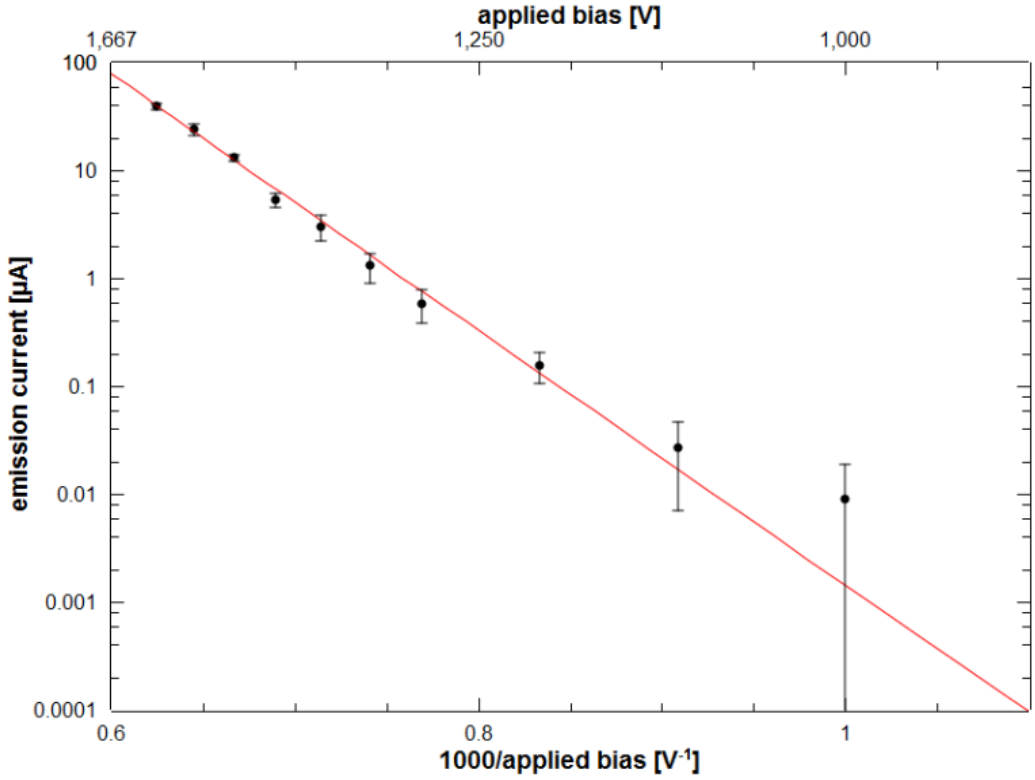

Fig. S2. Typical Fowler-Nordheim I-V plot. The red line is a linear fit of the experimental data using equation S3.

Fig. S2 depicts a typical Fowler-Nordheim I-V plot [ln(I) vs. V^{-1}]. The red line is a linear fit of the experimental data points. The field-emission characteristic I(F) for extended electrodes can be approximated by

$$I(F) = \left[v\left(\frac{F}{F_\phi}\right) - \frac{2}{3}\phi \right]^{-2} Aa\phi^{-1}F^2 \exp\left\{ -v\left(\frac{F}{F_\phi}\right) b\phi^{\frac{3}{2}}F^{-1} \right\} \quad \text{(S3)}$$

with $v\left(\frac{F}{F_\phi}\right)=1-\frac{F}{F_\phi}+\frac{1}{6}\frac{F}{F_\phi}\ln\frac{F}{F_\phi}$, and $F_\phi=\left(0.6944617 Vnm^{-1}\right)\left(\frac{\phi}{eV}\right)^2$ and the constants $a=1.541434\times10^{-6}\,AeVV^{-2}$ and $b=6.83089 eV^{-3/2}Vnm^{-1}$ (see Ref.[10]). ϕ is the work function of the cathode surface and A the emission area. The electric field, F, is given by the applied voltage divided by the separation of the electrodes, *d*. Defining an area-averaged value of the work function is a difficult task for a real surface with pointed structural features and a mixture of phases. We neglect such complications here and use the value 4.43 eV of bare Ag(100).[11] The only adjustable parameters in Eq. S3 are the emission area, A, and the gap separation, *d*. Fits to measured I-V curves yield typical values between 10^3 and 10^6 nm^2 for A, and 300 to 600 nm for *d*, respectively ($1.6\text{x}10^6$ nm^2 and 400 nm for the data shown in Fig. S2). These values indicate that the main emitters on the surface are particles, 200-500 nm in size, which locally reduce the gap separation. As the sample is transferred between the individual stages (sputtering, E-field, STM) several times per day, contamination of the single-crystal surface with small particles cannot be prevented completely. Especially the approach of the miniature electrode from above bears a certain risk that microparticles come off the linear motion mechanism and land on the sample surface. Ar^+ sputtering, which is the only method to clean the Ag(100) crystal surface in UHV, is very inefficient for removing particles. For example, hundreds of sputter cycles are required to completely remove a particle that is 300 nm in size.

While a large fraction of electrons is emitted at major surface asperities, at the highest voltages applied there is also a significant contribution to the total emission current from the smooth electrode areas. For U = 1500 V, inserting the nominal gap value d = 800 nm and the electrode area A = 15 mm^2 into Eq. S3, yields an emission current of 3.5 μA, which amounts to approximately 25% of the total emission current (see Fig. S2). From this current, which corresponds to a total number of $4\text{x}10^{16}$ electrons emitted during the 20 min exposure time (1 A = $6.241\text{x}10^{18}$ e^-/s), we can estimate a lower limit for the efficiency of the reduction process. The number of reduced NiO species is roughly $1\text{x}10^{14}$ (electrode area of 15 mm^2, NiO coverage of 0.7, the lattice parameter of Ag of 289 pm, and assuming that 90% of all NiO species got reduced in Fig. 1d) and, therefore, the reduction efficency is given by the number of reduced NiO species divided by the number of emitted electrons. It results an efficiency of 0.0025.

3. Comparison of AES spectra before and after electric-field experiments

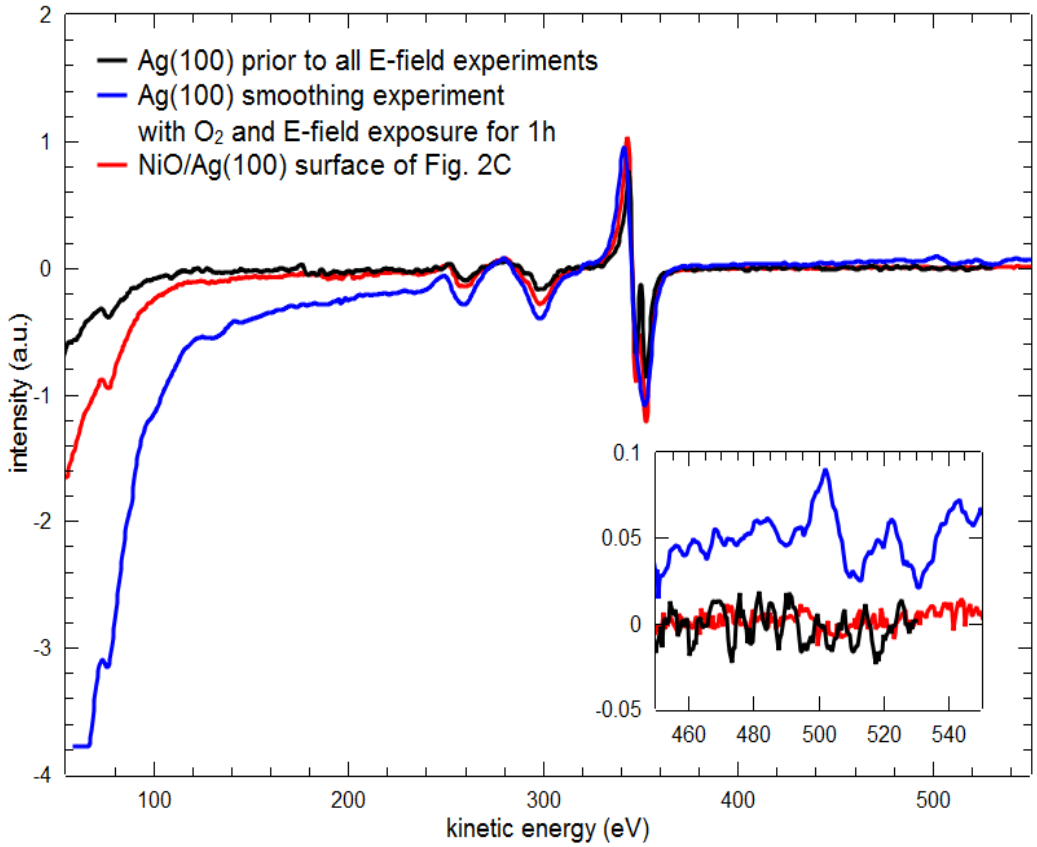

Fig. S3. Comparison of AES spectra. The black curve was recorded on the Ag(100) crystal prior to all electric-field experiments. The blue curve was recorded after exposure of the sputtered Ag(100) crystal to a strong electric field ($\dot{E}$ = 2 V/nm) in the presence of an oxygen atmosphere for one hour. The red curve was recorded on the reduced NiO/Ag(100) shown in Fig. 2c. The insert figure presents an enlarged view of the oxygen KLL peak region.

Figure S3 presents a comparison of AES spectra recorded before and after field experiments. The black curve was recorded on the cleaned Ag(100) crystal prior to all field experiments. It thus serves as a reference spectrum. The blue curve was recorded after exposure of the sputtered Ag(100) to a strong electric field ($\dot{E}$ = 2 V/nm) in the presence of an oxygen atmosphere for 1 h (total oxygen dose: 1200L). The red curve was recorded on the reduced NiO/Ag(100) surface shown in Fig. 2c. Compared to the black reference curve, no additional peaks are seen in the low-energy region of the blue and red curves. For example, in case of

Au contamination due to sputtering of the Au electrode, an additional peak would appear at around 85 eV, which is not the case.

The insert figure shows an enlarged view of the oxygen KLL region. The blue curves indicates the formation of AgO_x during field-exposure of the sputtered Ag(100) surface in the presence of an oxygen atmosphere. A faint oxygen KLL peak is also seen in case of the reduced NiO/Ag(100) surface (red curve).

4. Field-induced NiO reduction by an inhomogeneous electric field

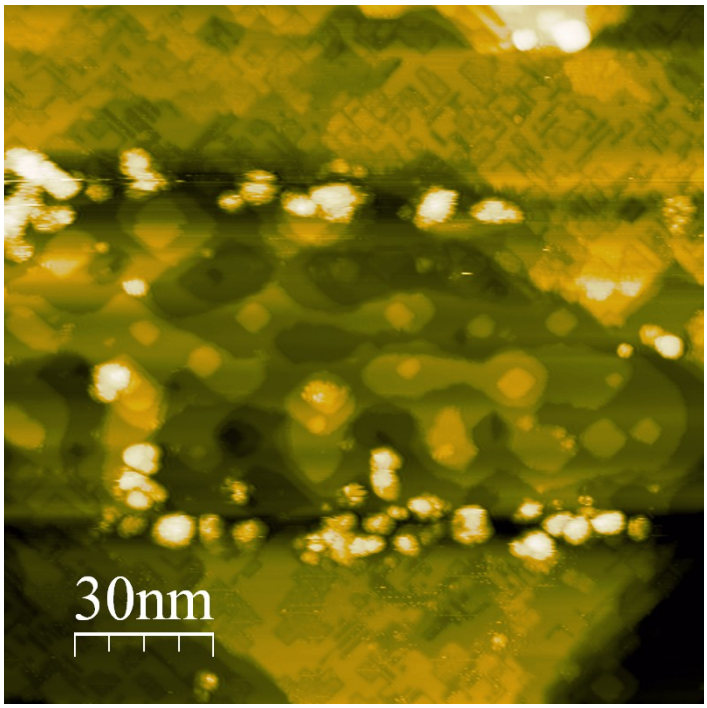

Fig. S4. STM image of a NiO(1x1)/Ag(100) "labyrinth phase" (see Ref. [1]) recorded after exposure to a strong electric field ($\vec{E}$ = 1 V/nm). Image details: 150x150 nm², U = 2 V, I = 100 pA.

Figure S4 depicts a STM image of a NiO(1x1)/Ag(100) "labyrinth phase" recorded after exposure to a strong electric field ($\vec{E}$ = 1 V/nm). The "labyrinth phase" is obtained by annealing the NiO(2x1) phase at 650 K (Ref. [1]). The image is characterized by a strong anisotropy. At the top and the bottom of Fig. S4, the "labyrinth phase" is still intact. In the middle part, the NiO phase is completely removed and the bare Ag surface is laid open. Large clusters (mean diameter 5 nm) are found at the borders between the unperturbed "labyrinth phase" and the reduced surface region.

The strong anisotropy seen in Fig. S4 is indicative of exposure to an inhomogeneous $\vec{E}$-field as it would occur in the proximity of surface asperities ("hot spots") for example. We have routinely recorded STM images on different locations on the sample that were exposed to the field without observing notable differences. Only on two or three occasions we happened to image surface regions that looked markedly different from Figs. 2 c,d. These areas displayed much larger clusters and showed a high degree of surface anisotropy like the one shown in Fig. S4.

Figure S4 also shows that field-induced NiO reduction is not limited to the (2x1) phase and that the threshold field-strength for observing NiO reduction is the same for both phases within the measurement uncertainty.

5. Electric-field promoted smoothing of Ag(100) in the presence of an oxygen atmosphere

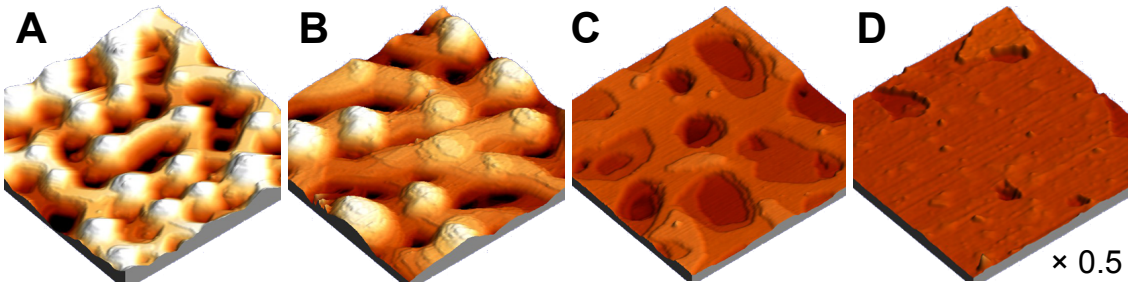

Fig. S5. Series of STM images recorded of a sputtered Ag(100) surface. (**A**) 5 min after sputtering, (**B**) 20 min after sputtering, (**C**) 4 h after sputtering and exposure to 4600L O_2 and (**D**) 4 h after sputtering and exposure to 4600L O_2 in the presence of a strong electric field ($\vec{E}$ = 2 V/nm). Image sizes: 150x150 nm² (**A-C**) and 300x300 nm² (**D**).

Figure S5 shows a series of STM images recorded on a sputtered Ag(100) surface at different times. Figures S5 A and B have been recorded 5 and 20 min after sputtering, respectively. Figures S5 C and D have been recorded after exposure of the sputtered crystal to 4600 L of oxygen, 4 h after Fig. S5 B; the region imaged in D has also been exposed to a strong electric field (2 V/nm).

The images reveal that at room temperature the initially rough Ag(100) smoothens already considerably due to surface diffusion of Ag. However, the characteristic formation of craters during sputtering does not disappear even after 4 h. Not shown here, the position of the first

maximum of the radially-averaged autocorrelation image for Figs. S4 A to C, which is a measure of the long-range order, shifts only marginally from 35 nm to 45 nm. In contrast, the surface region that was also exposed to a strong electric field does not possess a maximum of the radially-averaged autocorrelation image anymore, indicating that any long-range order is lost. In tune with this, the STM image shown in Fig. S5 D (demagnified by a factor of 0.5 compared to the other images) appears much smoother and exhibits only three silver height levels. However, a closer look at the big terrace reveals a high number of surface inhomogenities, which are presumably small AgO_x islands. This interpretation is supported by the AES spectrum (blue curve) shown in Fig. S3, which was recorded exposing the sputtered Ag(100) surface to a strong electric field-experiment and an oxygen atmosphere for one hour (compared to 4h for the STM image shown in Fig. S5 D).

6. Fiel-induced reduction of NiO nanostructures by an STM tip below -1.2 V

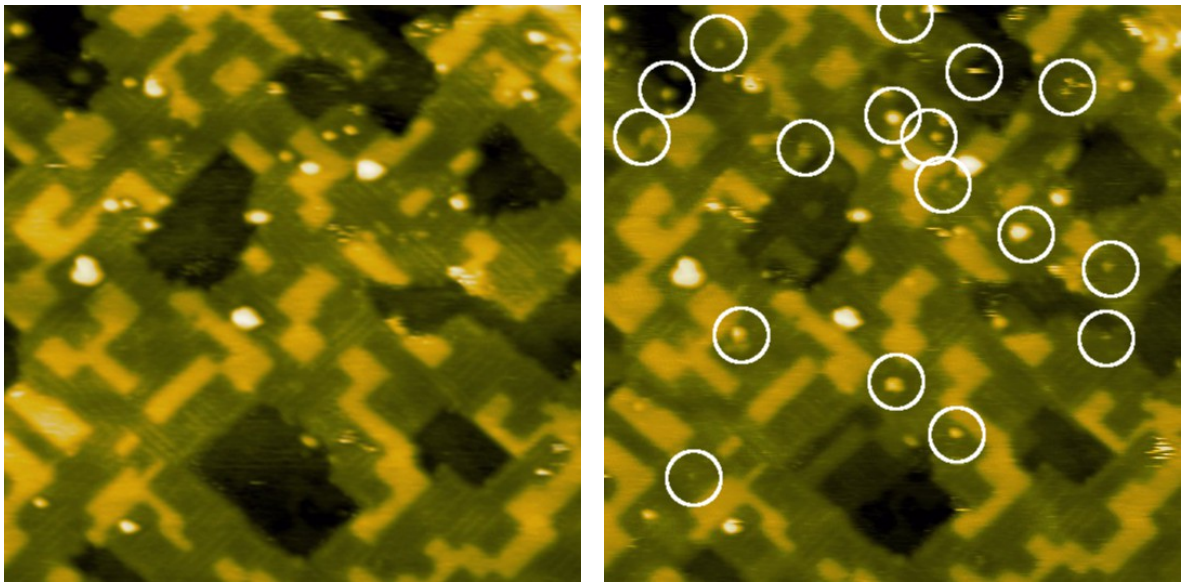

Fig. S6. Two consecutive scans of a NiO(2x1)/Ag(100) surface recorded by STM at a bias voltage of -2 V, I = 70pA; the frame size is 35x35nm². The white circles in the right panel highlight surface structural features that emerged from one scan to the next.

Figure S6 depicts two consecutive scans of a Ni(2x1)/Ag(100) surface recorded by STM at a bias voltage of -2 V. Like in the experiments performed with our homogeneous field apparatus, the influence of the tip (or better the tunneling current) manifests itself by the emergence of clusters (bright contrast), similar in size to the ones observed in Figs. 2c, d.

The white circles in the right image serve as a guide to the eye, highlighting the surface features that emerged from one scan to the next.

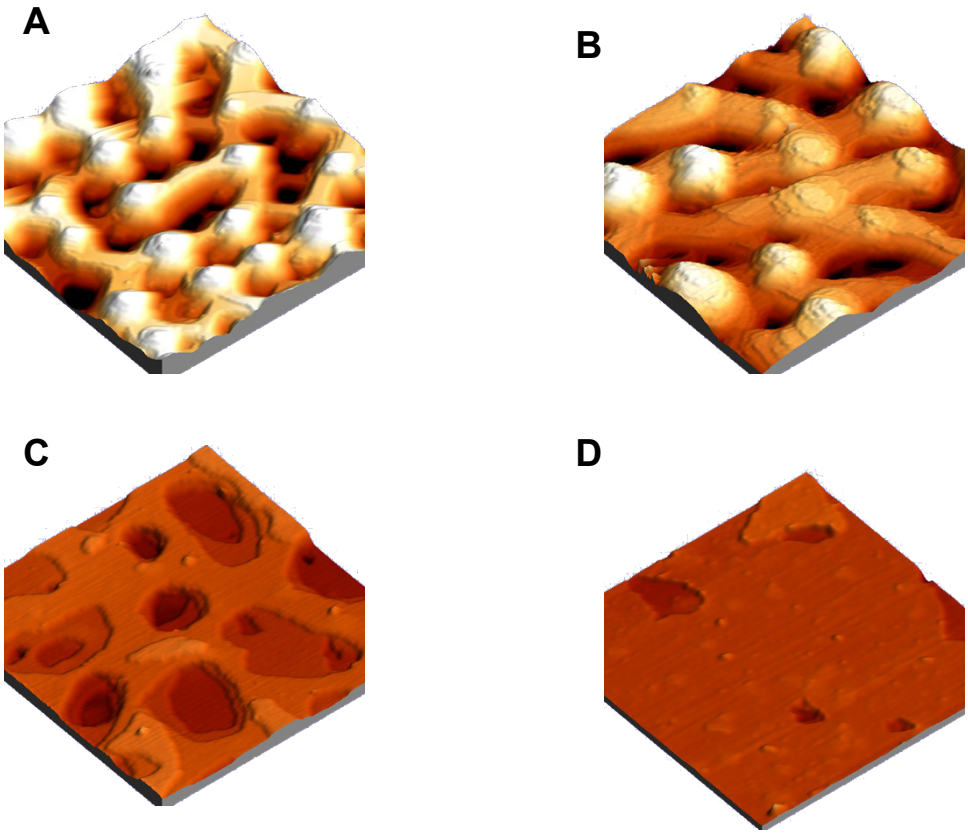

References

[1] W. Steurer, F. Allegretti, S. Surnev, G. Barcaro, L. Sementa, F. Negreiros, A. Fortunelli, F. P. Netzer, *Phys. Rev. B* **84**, 115446 (2011).

[2] P. Giannozzi, S. Baroni, N. Bonini, M. Calandra, R. Car, C. Cavazzoni, D. Ceresoli, G. Chiarotti, M. Cococcioni, I. Dabo, A. Dal Corso, S. De Gironcoli, S. Fabris, G. Fratesi, R. Gebauer, U. Gerstmann, C. Gougoussis, A. Kokalj, M. Lazzeri, L. Martin-Samos, N. Marzari, F. Mauri, R. Mazzarello, S. Paolini, A. Pasquarello, L. Paulatto, C. Sbraccia, S. Scandolo, G. Sclauzero, A. P. Seitsonen, A. Smogunov, P. Umari, and R. M. Wentzcovitch, *J. Phys.: Condens. Matter* **21**, 395502 (2009).

[3] D. Vanderbilt, *Phys. Rev. B* **41**, 7892 (1990).

[4] J. P. Perdew, K. Burke, and M. Ernzerhof, *Phys. Rev. Lett.* **77**, 3865, (1996).

[5] V. I. Anisimov, J. Zaanen, and O. K. Andersen, *Phys. Rev. B* **44**, 943 (1991).

[6] G. Barcaro, I. O. Thomas, and A. Fortunelli, *J. Chem. Phys.* **132**, 124703 (2010).

[7] L. Bengtsson, *Phys. Rev. B* **59**, 12301 (1999).

[8] H. Hogreve, *Int. J. Quantum Chem.* **109**, 1430 (2009).

[9] T. F. O'Malley, *Phys. Rev.* **150**, 14 (1966).

[10] R. G. Forbes, J. H. B. Deane, N. Hamid, H. San Sim, *J. Vac. Sci. Technol. B* **22,** 1342 (2004).

[11] S. Schuppler, N. Fischer, T. Fauster, W. Steinmann, *Phys. Rev. B* **46**, 13539 (1992).